VALIDATION OF A FINITE ELEMENT CODE FOR A CONTINUUM MODEL OF VOCAL FOLD VIBRATION UNDER THE INFLUENCE OF A SESSILE POLYP

Raymond Greiss [*1], **Joana Rocha** [†1], **and Edgar Matida** [‡1]
[1]Department of Mechanical and Aerospace Engineering, Carleton University, 1125 Colonel By Dr., Ottawa, Ontario, Canada, K1S 5B6

Abstract

Vocal fold vibration has been extensively investigated using numerical simulation through the use of lumped element models, and more recently, through the use of finite element continuum models. Finite element models offer the ability to analyze the effects of detailed and complex geometric models, allowing for the study of the influence of pathologies and phonosurgery on the process of phonation. The present study details the development of a finite element code of vocal fold vibration and a continuum model of a vocal fold with a sessile polyp. The capability of the code to capture major structural vibration trends are illustrated through a validation process, wherein previously explored models are replicated, and computed results are subsequently compared to gauge the code's efficacy. An overview of literature pertinent to the modeling of vocal fold polyps is presented, followed by the discussion of the creation of a continuum model of a vocal fold affected by a sessile polyp. This pathological model is parameterized according to the size and position of the polyp, and trends are explored based on varying these parameters. Polyp size is concluded to have a more profound influence on the fundamental frequency of vibration than position. An inversely proportional relationship is found between polyp size and fundamental frequency, as well as proximity to the anterior-posterior surface and fundamental frequency.

Keywords: Vocal fold, Polyps, Structural vibration, Finite element method

Résumé

Les vibrations des cordes vocales ont été étudiées extensivement par simulation numérique grâce à l'utilisation des modèles de paramètres localisés et, plus récemment, grâce à l'utilisation des modèles des éléments finis. Les modèles des éléments finis offrent la possibilité d'analyser les effets des modèles géométriques complexes et détaillés, facilitant ainsi l'étude de l'influence des pathologies et phonochirurgies sur le processus de phonation. Cette étude décrit le développement d'un code utilisant des éléments finis afin d'analyser les vibrations des cordes vocales. L'étude a aussi développé un modèle de continuum d'une corde vocale avec un polype sessile. La capacité du code à saisir les tendances importantes des vibrations structurelles est illustrée par un processus de validation, où des modèles existants sont répliqués et les résultats calculés sont comparés pour évaluer l'efficacité du code. Une révision de la littérature pertinente sur la modélisation des polypes sur les cordes vocales est présentée, suivie par une discussion sur la création d'un modèle de continuum d'une corde vocale avec un polype sessile. Ce modèle pathologique a été étudié en fonction de la taille et de la position du polype, et les tendances on été étudiées en fonction de ces paramètres. La taille du polype s'est avérée avoir une plus grande influence sur la fréquence fondamentale de la vibration que la position sur la corde vocale. Une relation inversement proportionnelle a été trouvée entre la taille du polype et la fréquence fondamentale, ainsi qu'une relation inversement proportionnelle entre la proximité de la surface antérieur-postérieur et la fréquence fondamentale.

Mots clefs: Cordes vocales, Polypes, Vibrations structurelles, Méthode des éléments finis

1 Introduction

Accurate simulation of structural vibration is dependent on a proficient formulation of a system's equation of motion. The proficiency of such a method is complex to assess for discrete models which are subject to numerous errors stemming from discretization, efficiency concerns, and representation of the physical system itself. Models of vocal fold vibration are susceptible to these issues, and as a result, multiple models have been developed which attempt to predict comparable vibration behaviour through various formulation techniques. These models have advanced with the introduction of continuum models [1–8], which distinguish themselves from traditional lumped element models [9–11] by virtue of their ability to incorporate the effects of complex spatial geometries on vibration behaviour. Notably, continuum models offer an avenue for detailed study of the effects of pathologies on vibration, such as polyps, nodules, and asymmetries.

An early and seminal two-mass lumped element model of vocal fold vibration was developed by Ishizaka and Flanagan [9]. This model approximated vocal folds as two masses coupled by springs and viscous dampers which were subject

∗. Raymondgreiss@cmail.carleton.ca
†. Joana.Rocha@carleton.ca
‡. Edgar.Matida@carleton.ca

to aerodynamic forces, modeled by Bernoulli flow. The model exhibited realistic self-oscillation properties previously observed only in experimental studies, such as the phase shift in motion between the upper and lower vocal fold edges [9, p. 1266]. The two-mass model was subsequently adopted for the study of the effect of pathologies on the generation of a speech signal, such as asymmetries [12–15] and polyps [16]. Though these models have generated comparable results to in-vivo studies, their use is limited to simulations which forfeit thorough physiological representation in exchange for computational efficiency. Developments of the two-mass model have, however, improved on spatial resolution and refined viscoelastic characterization [10, 11, 17].

Continuum models of laryngeal structure and flow have improved accuracy by virtue of refined and detailed discretization. One such complex vocal fold finite element (FE) model was developed by Alipour et al. [1], which considered a three-dimensional model of a vocal fold. This model uses distinct material properties for the body, cover, and ligament tissues, and approximates fluid interactions through Bernoulli flow. Oliveira Rosa et al. [2] expanded on this model by incorporating the entire larynx, adding longitudinal degrees of freedom, modeling tissue collisions, and modeling flow with the unsteady Navier-Stokes equations. Further extensions of the computational fluid-structure models have been made by incorporating the solution of the acoustic domain, as in [5], wherein a slightly compressible fluid model was used to capture the effects of the compressibility of air on acoustic wave propagation. Subsequent finite element method (FEM) models have examined pathological effects, including vocal trauma risk [18, 19], nodules [3], and asymmetries [20] which complement similar experimental studies [21]. Furthermore, continuum models provide the means for exploration of the governing physics of self-oscillation. Gunter [6] made use of a finite element vocal fold model to validate prediction of vocal fold closure forces and kinematics, drawing relationships between sub-glottal pressure and contact force, area of contact, and medial motion, followed by a similar experimental study [22]. Thomson [8] explored the mechanisms of aerodynamic energy transfer to the vocal folds through the use of both experimental and computational models, quantifying viscous effects and asymmetries in wall pressure due to cyclic vocal fold profile variations.

Advancement of computational vocal fold models requires consideration of realistic geometric and viscoelastic characterization. One such study deviates from the use of idealized vocal fold geometries through generation of a mesh using MRI image slices and various tissue property values [4]. In addition, experimental determinations of vocal fold material property value ranges have been performed to improve the characterization of vocal fold layer anisotropy [23]. The necessity of these realistic models has been explored through sensitivity studies, which asses the effects of both geometric and material idealizations in computational models on mechanical response. Shurtz and Thomson [7] perform one such study in which they assess the effects of the vocal fold collision contact line position, Poisson ratio, and symmetry conditions on the fluid and structural response.

Overall, these computational models of vocal fold vibration have illustrated the ability to predict similar trends of vibration which agree with experimental studies. A natural progression in improving these models is the investigation of the effects of pathologies on these trends, specifically, with detailed modeling of the pathological geometry. The following study is an attempt to validate an in-house FE formulation of the vibration of vocal folds affected by a sessile polyp which is resolved with an in-house solver. This validation is performed as part of the development of a predictive tool intended for further investigations of the effects of pathological tissue on vocal fold vibration. The FE method is used to formulate the equation of motion of the system, and considering free vibration conditions, resolve the system for natural frequencies and mode shapes. These results are subsequently compared with investigations by [24–26]. This validation process is critical for future investigations which will make use of this tool, since experimental data for pathological speech may not provide a precise metric as a comparison.

2 Discretization and Structural Modeling

The equations of motion of a physical system may be derived using Hamilton's principle, which states

$$\int_{t_1}^{t_2} (\delta(T-U) + \delta W_{nc})\mathrm{d}t = 0 \tag{1}$$

where t_1 and t_2 represent time at two distinct points, δ denotes a virtual variable, T is the kinetic energy of the system, U is the strain energy of the system, and W_{nc} represents the work done to the system by non-conservative forces [27, p. 9]. This principle describes the path of a conservative system between two discrete positions given the system's scalar energy functions. For discretized systems, equation (1) can be simplified using Lagrange's equations, given by

$$\begin{aligned} \left\{ \frac{\partial}{\partial t}\left(\frac{\partial T}{\partial \dot{q}(t)}\right)\right\} &= [M]\{\ddot{q}(t)\} \\ \left\{\frac{\partial D}{\partial \dot{q}(t)}\right\} &= [C]\{\dot{q}(t)\} \\ \left\{\frac{\partial U}{\partial q(t)}\right\} &= [K]\{q(t)\} \end{aligned} \tag{2}$$

where $\{q(t)\}$ is a vector of system displacements, $\{\dot{q}(t)\}$ is a vector of system velocities, $\{\ddot{q}(t)\}$ is a vector of system accelerations, $[M]$ is the matrix of inertia, D is a dissipation energy function, $[C]$ is the damping matrix, and $[K]$ is the matrix of stiffness [27, p. 13]. The set of Lagrange's equations can be used to develop the equation of motion for the discrete system given the scalar energy functions, which is given by

$$[M]\{\ddot{q}(t)\} + [C]\{\dot{q}(t)\} + [K]\{q(t)\} = \{F\} \tag{3}$$

where $\{F\}$ is the vector of applied non-conservative forces on the system. For the present study, discrete systems under free-vibration are considered. Free-vibration conditions ignore damping and applied forces. Substituting these conditions into equation (3),

$$[M]\{\ddot{q}(t)\} + [K]\{q(t)\} = 0. \tag{4}$$

This system of equations can be developed by evaluating equation (2) given the kinetic and strain energy functions of the system.

The kinetic energy function for a general three-dimensional solid is given by

$$T = \frac{1}{2}\int_V \rho(\dot{u}^2 + \dot{v}^2 + \dot{w}^2)\mathrm{d}V \tag{5}$$

where V is the volume of the solid, ρ is the density, and u, v, and w represent displacement components in x,y,z Cartesian space, respectively [27, p. 39]. The strain energy function for a general three-dimensional solid is given by

$$U = \frac{1}{2}\int_V \{\epsilon\}^T [D] \{\epsilon\} \mathrm{d}V \tag{6}$$

where $\{\epsilon\}$ is the strain component vector given by

$$\{\epsilon\}^T = \left\{\frac{\partial u}{\partial x}, \frac{\partial v}{\partial y}, \frac{\partial w}{\partial z}, \frac{\partial u}{\partial y} + \frac{\partial v}{\partial x}, \frac{\partial u}{\partial z} + \frac{\partial w}{\partial x}, \frac{\partial v}{\partial z} + \frac{\partial w}{\partial y}\right\}, \tag{7}$$

and $[D]$ is the stiffness matrix of the solid, which can be computed as the inverse of the compliance matrix given by Hooke's law for linearly elastic materials [27, p. 38]. For systems with varying boundary conditions or complex geometries, the energy functions are difficult to derive analytically, and accordingly, the Finite Element Displacement Method (FEDM) is used to approximate each function over discrete volumes of space.

The FEDM approximates the energy functions over elements, which are defined by a collection of Cartesian nodal coordinates, represented as the column vectors $\{u\}_e$, $\{v\}_e$, $\{w\}_e$. Each node of the element, unless constrained by a boundary condition, has three translational degrees of freedom. These displacement and velocity components are approximated by shape functions, and subsequently used to evaluate equations (5) and (12). For an element defined by n nodes, there must exist n shape functions. Each shape function must have a value of unity at its corresponding node, and a value of zero at all other nodes. Displacement functions can be defined based on the set of shape functions, $[N]$, and the nodal coordinates,

$$\begin{aligned} u &= [N]\{u\}_e \\ v &= [N]\{v\}_e \\ w &= [N]\{w\}_e \end{aligned} \tag{8}$$

or

$$\begin{Bmatrix} u \\ v \\ w \end{Bmatrix} = [N]\{q(t)\}_e \tag{9}$$

Equation (9) can be substituted into equations (5) and (12) and integrated, resulting in

$$\begin{aligned} T_e &= \tfrac{1}{2}\{\dot{q}(t)\}_e^T [m]_e \{\dot{q}(t)\}_e \\ U_e &= \tfrac{1}{2}\{q(t)\}_e^T [k_e \{q(t)\}_e \end{aligned} \tag{10}$$

where $[m]_e$ is the inertia matrix of the element and $[k]_e$ is the stiffness matrix of the element [27, pp. 103-104]. Rearranging equation (10),

$$\begin{aligned} [m]_e &= \textstyle\int_{V_e} \rho[N]^T[N]\mathrm{d}V \\ [k]_e &= \textstyle\int_{V_e} [B]^T[D][B]\mathrm{d}V \end{aligned} \tag{11}$$

where $[B]$ is the strain matrix of the form [27, p. 200]

$$[B] = \begin{bmatrix} \frac{\partial N_1}{\partial x} & 0 & 0 & \cdots & \frac{\partial N_n}{\partial x} & 0 & 0 \\ 0 & \frac{\partial N_1}{\partial y} & 0 & \cdots & 0 & \frac{\partial N_n}{\partial y} & 0 \\ 0 & 0 & \frac{\partial N_1}{\partial z} & \cdots & 0 & 0 & \frac{\partial N_n}{\partial z} \\ \frac{\partial N_1}{\partial y} & \frac{\partial N_1}{\partial x} & 0 & \cdots & \frac{\partial N_n}{\partial y} & \frac{\partial N_n}{\partial x} & 0 \\ \frac{\partial N_1}{\partial z} & 0 & \frac{\partial N_1}{\partial x} & \cdots & \frac{\partial N_n}{\partial z} & 0 & \frac{\partial N_n}{\partial x} \\ 0 & \frac{\partial N_1}{\partial z} & \frac{\partial N_1}{\partial y} & \cdots & 0 & \frac{\partial N_n}{\partial z} & \frac{\partial N_n}{\partial y} \end{bmatrix}. \tag{12}$$

Equation (11) is evaluated for each element based on the given nodal coordinates and shape functions. The elemental inertia and stiffness matrices are subsequently added to the global equation of motion, equation (4). The global equation of motion is fully assembled once all elemental inertia and stiffness matrices are computed and added to the equation.

2.1 Tetrahedral shape functions

The evaluation of equation (11) can be performed analytically for a four-node tetrahedron because the entries in $[N]$ are constants, and consequently, result in constant strain entries in $[B]$. Accordingly, the four-node tetrahedral elements are called "constant strain elements". Equation (11) was derived analytically for the constant strain elements using the Matlab symbolic toolbox [28], and subsequently evaluated as functions of the nodal coordinates. The ten-node tetrahedron elements have linear strain entries in $[B]$, and accordingly, require a numerical integration method to evaluate equation (11). Consequently, "linear strain elements" will approximate strain gradients more accurately than the constant strain elements, in exchange for computational efficiency.

2.2 Numerical integration of elemental inertia and stiffness matrices

Evaluation of equation (11) for linear strain elements was performed with four-point Gauss-Legendre quadrature. This integration scheme approximates a definite integral through the sum of weighted samples within the domain of integration. For a definite integral I, [29, p. 373]

$$\begin{aligned} I &= \int_0^1 \int_0^{1-\zeta_1} \int_0^{1-\zeta_1-\zeta_2} f(\zeta_1,\zeta_2,\zeta_3,\zeta_4)\mathrm{d}\zeta_3\mathrm{d}\zeta_2\mathrm{d}\zeta_1 \\ &= \sum_{i=1}^{4} H_i f(\zeta_1,\zeta_2,\zeta_3,\zeta_4) \end{aligned} \tag{13}$$

where f is the integrand of equation (11), and H_i is a weight applied for sample point i, called the ith "Gauss point" [30, p. 200].

2.3 Solution of the global eigensystem

Once the global mass and stiffness matrices have been assembled, the solution to equation (4) can be computed. The solution is assumed to be of the form

$$u = \phi \sin \omega(t - t_0) \tag{14}$$

where ϕ is an eigenvector of the system, ω is the corresponding frequency of vibration, t is the time variable, and t_0 is a time constant [31, p. 786]. Substituting equation (14) into equation (4), the generalized eigensystem may be expressed

$$[K]\phi = \omega^2[M]\phi, \tag{15}$$

which for an N degree of freedom system yields N pairs of eigenvector, ϕ, and eigenvalue, ω^2, solutions [31, p. 786].

The code was developed to solve the general eigensystem expressed in equation (15). The specifics of the model are input to the solver as the mesh, boundary conditions, and material properties. Once the local inertia and stiffness matrices are generated for each element and subsequently mapped to the global system, the global eigensystem is solved for its eigenvectors and eigenvalues.

3 Validation case 1

The computer program STARS (STructural Analysis RoutineS) was developed by NASA in the 1980's for the purpose of analyzing the static, stability, free-vibration, and dynamic responses of structural systems [24, p. 1]. The documentation which accompanies the software gives several sample problems to illustrate its capabilities. One such problem investigated is the free-vibration of a three-dimensional isotropic cube which is fixed at one face, as shown in Figure 1. Each of the free nodes within the model have three translational degrees of freedom. This same problem is considered as the first validation case. The relevant parameters of the simulation are provided in Table 1.

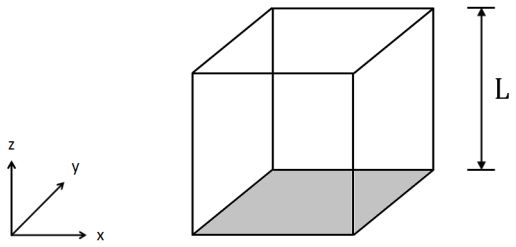

Figure 1: Physical system under consideration for the first validation case. The gray face is fixed, while the transparent faces are free.

To compare the solutions for natural frequencies obtained computationally with the exact solution provided in [24, p. 42], the solutions are normalized according to the following equation :

$$\bar{\omega_i} = \frac{\omega_i}{\sqrt{E/\rho}} \tag{16}$$

Table 1: Physical parameters for the first validation case [24, p. 41]

Parameter	Value (dimensionless)
Side length, L	10
Young's Modulus	10×10^{-6}
Poisson's ratio	0.3
Density	2.349×10^{-4}

where $\bar{\omega_i}$ is the ith normalized form of the ith natural frequency, ω_i.

Convergence behaviour of both the constant strain and linear strain finite element models were investigated by calculating the normalized natural frequencies of the cube for increasingly refined mesh sizes. This behaviour is illustrated in Figure 2. Both models show gradual convergence towards the exact solution, with the linear strain elements approaching the solution at a faster rate than the constant strain elements. Linear strain elements improve accuracy through the use of quadratic shape functions, which results in variable derivatives of the shape functions over the element volume [29, p. 335] which better approximate strain gradients.

A direct comparison of the computationally obtained non-dimensional natural frequencies for both the constant and linear strain elements is shown in Table 2. Linear strain elements show superior accuracy for the first six modes compared to the constant strain model. The percent error lies below 2.6 % and 10.3 % of the exact solution for the linear strain model and constant strain models, respectively. Accordingly, high accuracy solutions may be obtained with a larger number of constant strain elements than linear strain elements. In the following validation cases, the selection between either of these element types will consider this balance of accuracy and efficiency.

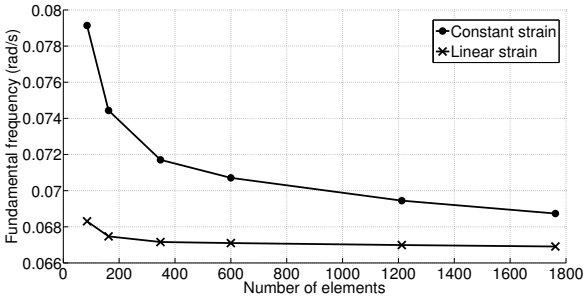

Figure 2: Convergence behaviour of the finite element solution for both constant strain and linear strain elements.

4 Validation case 2

An early continuum model of vocal fold vibration is documented in [25]. This model approximates a single vocal fold as a parallelepiped with three fixed faces representative of the anterior, posterior, and lateral surfaces, as shown in Figure 3. The free-vibration of this model is considered as the second validation case. Relevant physical parameters are tabulated in

Table 2: Comparison of exact natural frequency solution from [24] with developed model for constant and linear strain elements

(a) Constant strain

Mode number	Exact solution	Computed solution	Percent error (%)
1	0.0680	0.0707	4.00
2	0.0680	0.0710	4.35
3	0.0929	0.1024	10.25
4	0.1611	0.1629	1.09
5	0.1819	0.1887	3.74
6	0.1819	0.1890	3.92

(b) Linear strain

Mode number	Exact solution	Computed solution	Percent error (%)
1	0.0680	0.0671	1.34
2	0.0680	0.0672	1.25
3	0.0929	0.0912	1.82
4	0.1611	0.1600	0.69
5	0.1819	0.1772	2.60
6	0.1819	0.1772	2.57

Table 3. The plane of isotropy is in the vertical-lateral plane, while the anterior-posterior direction represents the longitudinal direction with distinct material parameters. The nodes of the model have translational degrees of freedom in the vertical and lateral directions, while anterior-posterior translations are assumed negligible.

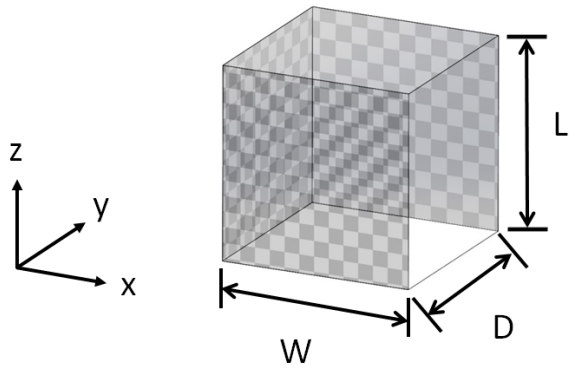

Figure 3: Physical system under consideration for the second validation case. Textured faces are fixed, while the transparent faces are free. x-direction : Lateral. y-direction : Anterior-posterior. z-direction : Vertical.

Table 3 shows two values for the transverse Poisson's ratio. Case 2a represents the completely compressible case, and case 2b represents the nearly incompressible case. The variation of this parameter was shown to alter the computed mode shapes in [25], and accordingly, will be considered as two separate cases as part of the following validation. For each case, the first three natural frequencies and mode shapes are computed, and compared with the results in [25].

Table 3: Physical parameters for the second validation case [25, p. 3349]

Parameter	Value	
Lateral depth, W	1.0 cm	
Longitudinal (anterior-posterior) length, D	1.2 cm	
Vertical thickness, L	0.7 cm	
Density	1.03 g/cm^3	
Transverse Young's modulus	10^5 dyn/cm^2	
Longitudinal shear modulus	10^5 dyn/cm^3	
Transverse Poisson's ratio	Case 2a 0	Case 2b 0.9999
Longitudinal Poisson's ratio	0	

4.1 Case 2a : Completely compressible case

Convergence behaviour of the model's first three natural frequencies for the compressible case are displayed in Figure 4. Asymptotic behaviour is observed for nearly all model sizes, which illustrates that the purely lateral vibration behaviour requires a model with low resolution to produce accurate predictions of natural frequencies. The predicted natural frequencies entrain on the ranges reported in [25], with numerical values and percent differences tabulated in Table 4. Exact values are not reported in [25] ; accordingly, values were approximated through a digital image extraction from reported plots.

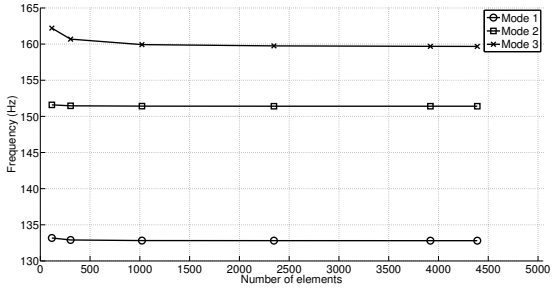

Figure 4: Convergence of the first three natural frequencies of the completely compressible validation case.

Table 4: Comparison of computed natural frequencies for the completely compressible validation case

Mode number	Computed frequency (Hz)	Frequency from [25] (Hz)	Percent difference (%)
1	132.8002	132.8	0.0002
2	151.4063	151.5	0.0619
3	159.7	159.6	0.048

A qualitative comparison of the predicted mode shapes in the mid-coronal plane are illustrated in Figure 5. This figure illustrates that the predicted mode shapes of the present investigation are in general agreement with those from [25].

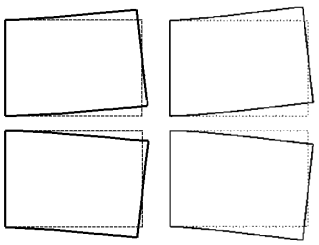

(a) Mode shape 1

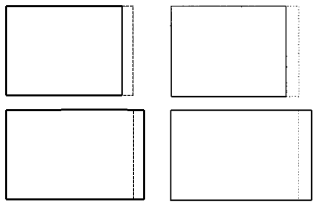

(b) Mode shape 2

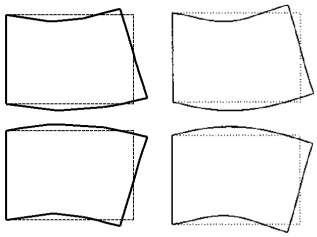

(c) Mode shape 3

Figure 5: Comparison of mode shapes for the completely compressible case. Left : Computed mode shape. Right : Mode shape from [25].

4.2 Case 2b : Nearly incompressible case

Convergence behaviour for the nearly incompressible case is displayed in Figure 6. Asymptotic behaviour is not observed for lower resolution models as in the compressible case, and accordingly, only higher resolution models yield comparable results. Natural frequencies once again entrain on the values reported in [25], with a numerical comparison given in Table 5. Percent differences are larger for the nearly incompressible model than for the completely compressible model. This is likely due to the influence of the transverse vibration introduced due to the change in the transverse Poisson's ratio. Despite this deviation, percent differences are low, with differences peaking at 1.7451 %.

Table 5: Comparison of computed natural frequencies for the nearly incompressible validation case

Mode number	Computed frequency (Hz)	Frequency from [25] (Hz)	Percent difference (%)
1	133.2423	132.4	0.6342
2	153.7600	151.1	1.7451
3	155.3512	152.8	0.048

A qualitative comparison of the predicted mode shapes on the mid-coronal plane are illustrated in Figure 7. This figure illustrates that the predicted mode shapes of the present

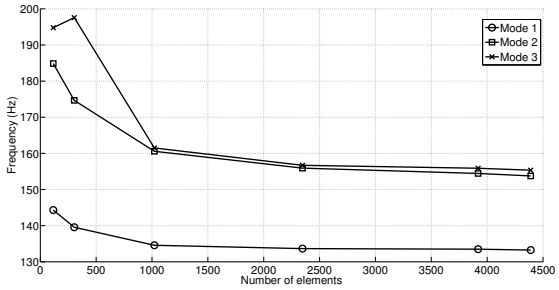

Figure 6: Convergence of the first three natural frequencies of the nearly incompressible validation case.

investigation are in general agreement with those from [25].

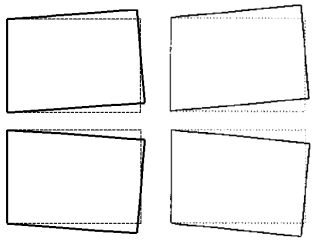

(a) Mode shape 1

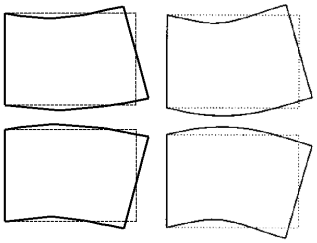

(b) Mode shape 2

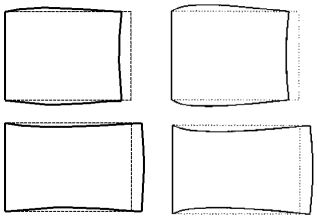

(c) Mode shape 3

Figure 7: Comparison of mode shapes for the nearly incompressible case. Left : Computed mode shape. Right : Mode shape from [25].

5 Validation case 3

A model of a multi-layered continuum model of a vocal fold is documented in [26]. This model clearly defines the division of the vocal fold into distinct body, cover, and ligament regions, each with its own material property values. These values are reported in Table 6. The geometry of the model is illustrated in Figure 8, however, detailed geometric considerations are reported in full in [26, p. 9330]. Similar to the second validation case, the vocal fold was fixed along the anterior-

posterior surfaces, and the lateral surface. Free nodes of the model were allowed three translational degrees of freedom. The material was treated as transversely isotropic, with the transverse plane in the x-y direction.

Table 6: Physical parameters for the third validation case [26, p. 9316]

Parameter	Body	Cover	Ligament
Transverse shear modulus (kPa)	1.05	0.53	0.87
Longitudinal shear modulus (kPa)	12	10	40
Longitudinal Young's modulus (kPa)	31.2	26	104
Transverse Poisson ratio	0.3	0.3	0.3
Longitudinal Poisson ratio	0.3	0.3	0.3
Density (g/cm^3)	1.0	1.0	1.0

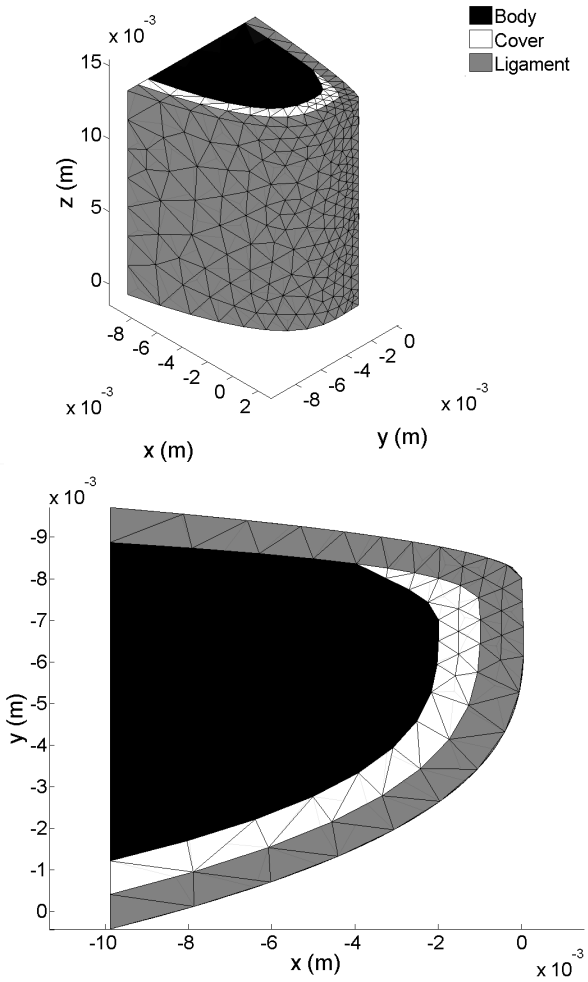

Figure 8: Physical system under consideration for the third validation case. The anterior-posterior faces (x-y surfaces) and the lateral face (x-z surface) are fixed, while the remaining nodes have three translational degrees of freedom.

Convergence behaviour of the model is shown in Figure 9. A large number of elements are required to approach convergence. Accordingly, constant strain elements were used for the analysis in order to preserve efficiency due to an inherently large requirement of degrees of freedom. A comparison of the first four computed natural frequencies is reported in Table 7. The percent differences are minimal, which indicates that the converged solution agrees with the reported values in [26].

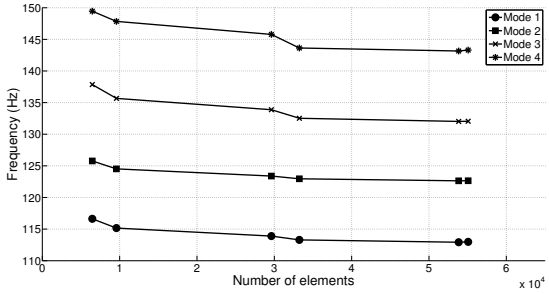

Figure 9: Convergence of the first four natural frequencies of the third validation case.

Table 7: Comparison of computed natural frequencies for the third validation case

Mode number	Computed frequency (Hz)	Frequency from [26] (Hz)	Percent difference (%)
1	112.9847	114	0.90
2	122.6436	125	1.90
3	132.0509	133	0.72
4	143.3063	144	0.5

A qualitative comparison of the first four mode shapes is illustrated in Figure 10. Similar to the second validation case, pictured is the periphery of the mid-coronal plane of the vocal fold. Solid and dashed lines represent the positive and negative eigenvector mode shapes respectively. General agreement is shown between the modes, with the exception of the third mode shape. In Figure 10c, a slight difference between the y-component of magnitude can be seen, as parts of the overlapping mode shapes show dissimilarity. This difference may be attributed to the method in which the mode shape was calculated, or slight differences in modeling the vocal fold geometry.

6 Modeling of a polyp

The following analysis is concerned with the documentation of the development of a continuum model of a vocal fold with a unilateral sessile polyp. Similar continuum models of vocal fold polyps [3, 32] have been developed, and accordingly, the trends discussed in these studies will be compared. The model presented herein is concerned with accurate representation of the polyp shape, material behaviour and position on the vocal fold.

6.1 Polyp pathology

Vocal fold polyps are benign lesions [33] which form on the superficial layer of the vocal fold. These lesions are typically unilateral, meaning they appear on one fold only [34, p. 456],

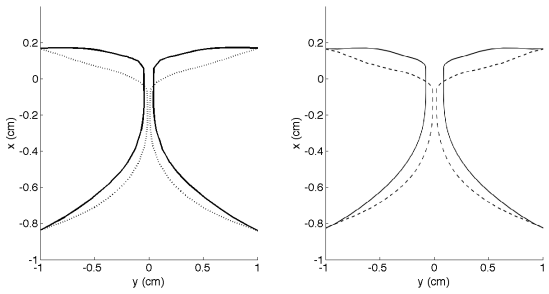

(a) Mode shape 1

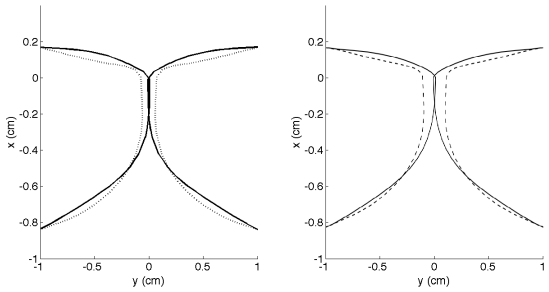

(b) Mode shape 2

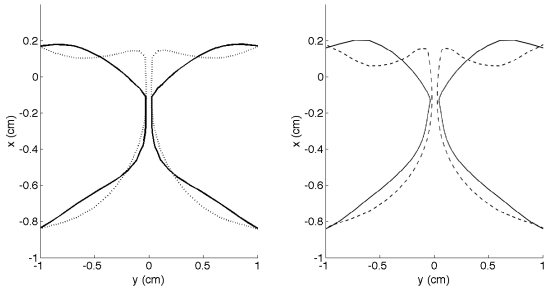

(c) Mode shape 3

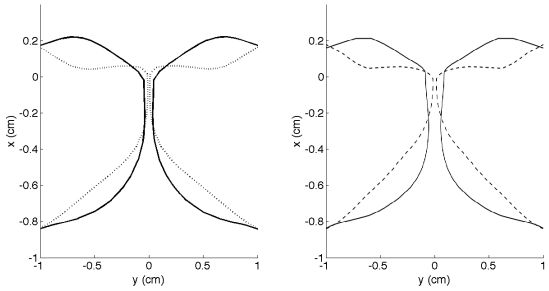

(d) Mode shape 4

Figure 10: Comparison of mode shapes for the third validation case. Left : Computed mode shape. Right : Mode shape from [26].

or they may be bilateral, pedunculated, or sessile [33]. Due to the additional mass, increased stiffness, and damping properties of the polyp, as well as the influence of a gelatinous material which forms on the sub-epithelial layer of the vocal fold [33], mucosal wave propagation is altered on the vocal fold, and voice disorders may arise as a result [21, pp. 93-94]. The sessile polyps often manifest as half ellipses which protrude from the medial surface of the fold [35, p. 268]. Based on this data, the sessile polyp in this model is based on half of a sphere which protrudes from the medial surface of the vocal fold. The sphere's center is placed at the vertical midpoint of the surface, on top of the cover layer of the vocal fold. The polyp's center may be moved along the anterior-posterior direction to simulate asymmetries. In [36], a clinical study was performed which observed polyps as large as 0.7 mm in length, width, and depth. Accordingly, the half-spherical polyp modeled in this study may have a length bounded between 0.3 mm and 0.7 mm.

The material properties of polyps have a wide range of reported values. The typical trend, however, is an increase in stiffness relative to the surrounding vocal fold muscle tissue. In [32], polyp tissue is simulated as a five-fold increase in stiffness. The same assumption is made of the polyp modeled in the present study. The polyp will also be assumed to be isotropic, as there exist no muscle fibers which run through the lesion resulting in transverse isotropy. Subsequently, the Young's modulus of the polyp is assumed to be five times the longitudinal stiffness of the vocal fold ligament, with a Poisson's ratio of 0.3, and the same density as the surrounding tissue.

6.2 Model parameters and simulation setup

The vocal fold geometry described in [26] is adopted for this study, as it sufficiently details the geometry and material properties of a multi-layered vocal fold. The illustration in Figure 11 displays this model with the addition of a 0.7 mm diameter polyp centered along the anterior-posterior direction. The material properties of this model are given in Table 6 and Table 8.

Table 8: Unilateral sessile polyp model parameters

Parameter	Value
Young's Modulus (kPa)	520
Poisson ratio	0.3
Density (g/cm^3)	1.1

For the purpose of this investigation, trends related to the position and size of the polyp will be explored. In [3], the effect of varying these parameters of a point mass nodule on the fundamental frequency of the vocal fold are determined. This study concluded that fundamental frequency decreased as the polyp size increased, and that the fundamental frequency decreased as the polyp approached the center of the anterior-posterior direction. This analysis is repeated with a spatially modeled polyp in order to compare trends. Accordingly, two sets of simulations are run. The first set of five simulations varies the polyp length, s, between 0.3 mm $\leq s \leq$ 0.7 mm in 0.1 mm increments. Figure 12 illustrates the two extreme cases run in this set of simulations. The second set of simulations varies the position of a 0.7 mm polyp along the anterior-posterior direction. Ten positions centered between 0.7 mm and 7 mm along the right side of the vocal fold are selected. By virtue of symmetry, polyps are not placed on the left side of the vocal fold, as computed frequencies would expected to

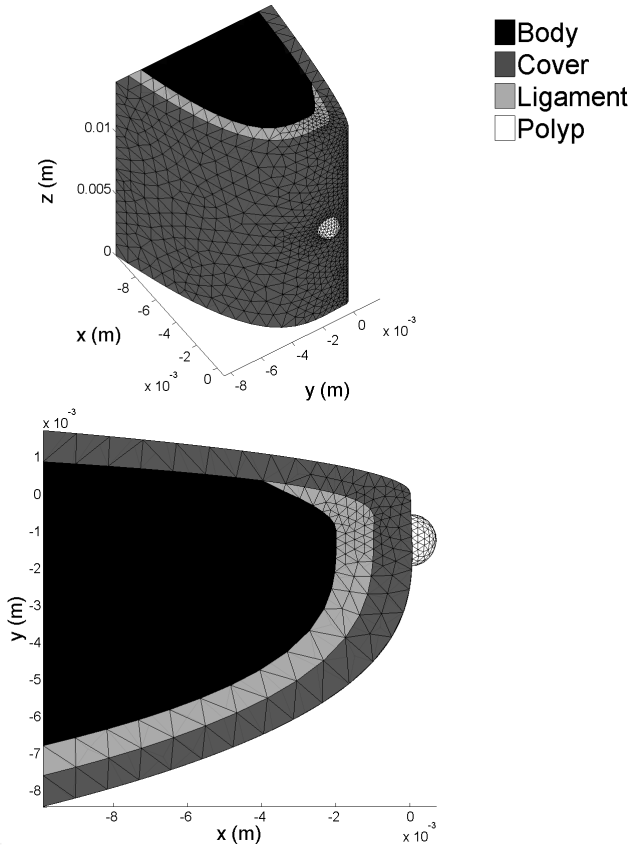

Figure 11: Mesh of a vocal fold with a sessile polyp.

be replicated. Figure 13 illustrates the two extreme cases in the second set of simulations.

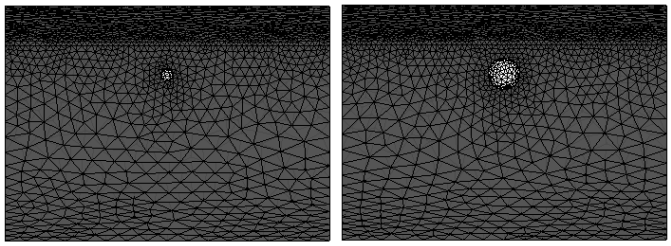

(a) $s = 0.3$ mm and $c = 7$ mm. **(b)** $s = 0.7$ mm and $c = 7$ mm.

Figure 12: Illustration of extreme cases of the first set of simulations. Holding $c = 7$ mm, the polyp size is varied.

7 Results

The first set of simulations was used to generate data to define a relationship between the fundamental frequency of the pathological vocal fold and polyp size, which is illustrated in Figure 14. This figure shows that, similar to [3], an inverse proportionality exists between the fundamental frequency and the polyp size. Asymptotic behaviour can be observed for the largest and smallest polyps. Small polyps have a negligible effect on the fundamental frequency, indicating that the small

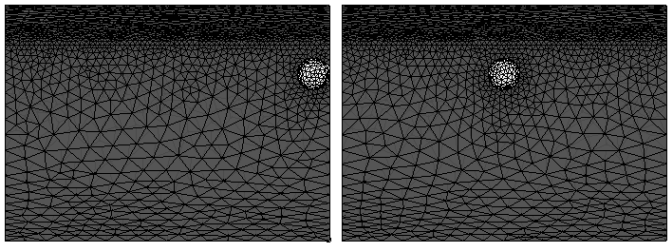

(a) $c = 0.7$ mm and $s = 0.7$ mm. **(b)** $c = 7$ mm and $s = 0.7$ mm.

Figure 13: Illustration of extreme cases of the second set of simulations. Holding $s = 0.7$ mm, the polyp position is varied.

localized change in mass and stiffness has little influence on the natural frequency. Inversely, for large polyps, a more substantial region of the vocal fold is affected by the mass and stiffness change, and consequently, the rate of decrease of the fundamental frequency is significant.

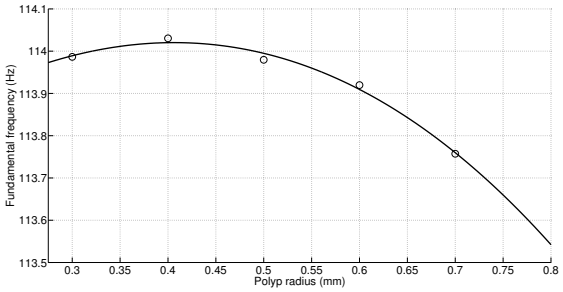

Figure 14: Relationship between vocal fold size and fundamental frequency of the pathological vocal fold.

The results of the second set of simulations can be used to show that when the polyp is centered along the anterior-posterior direction, fundamental frequency is minimized. This relationship is illustrated in Figure 15. A linear trend was fitted to this data, which indicates that anterior-posterior position of the polyp may not have as profound of an influence on the natural frequency as the polyp size. Due to symmetry, a mirror image of this plot would be expected for samples between 7 mm $\leq c \leq$ 17 mm.

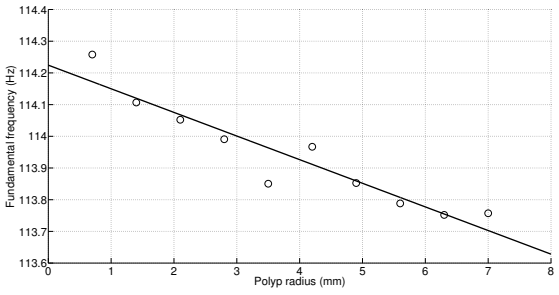

Figure 15: Relationship between vocal fold position and fundamental frequency of the pathological vocal fold.

The non-linear relationship between polyp size and fun-

damental frequency is the result of adding an increasing volume of stiff material to the vocal fold. Since the parameter s is a measure of polyp length, increasing s by a factor of n results in the increase of polyp volume by a factor of n^3. This addition of mass and stiffness to the overall system results in a sharp decrease in fundamental frequency. Due to the influence of the zero degree of freedom boundary conditions at the anterior and posterior surfaces of the vocal fold, the excess mass and stiffness of the polyp have less of an effect on fundamental frequency near these surfaces. Consequently, the minimization of fundamental frequency occurs when the polyp manifests at the center of the vocal fold, where the excess mass and stiffness of the polyp has more influence on the overall system.

8 Conclusions

The validation process of the preceding finite element code is a necessary procedure to ensure accurate prediction of structural vibration behaviour for pathological vocal fold models. This process was documented through direct comparison of natural frequencies and mode shapes for several different models of varying complexity, including various orthotropic material conditions, boundary conditions, and complex geometries. These quantitative and qualitative comparisons show good agreement, indicating that the code is suitable for use as a predictive tool. The tool was subsequently tested through the solution of a model of a vocal fold affected with a unilateral sessile polyp which illustrated the expected trends of fundamental frequency variation with polyp size and position.

The model of a unilateral sessile polyp presented in this study is an attempt at modeling a pathology in a continuum medium. Polyp size, material properties, position, and geometry were considered based on a literature survey of clinical data, in some cases with upper and lower bounds presented to account for tissue variation across multiple specimens. This model was validated by considering two sets of simulations which assessed the effect of polyp size and position on the fundamental frequency of the system. The results presented in this study show agreement with previous investigations of the same relationships. Increasing the length of the half-spherical polyp was shown to result in a non-linear decrease in fundamental frequency due to the corresponding exponential increase in mass and stiffness in the model. Polyp position was shown to vary the fundamental frequency linearly along the medial plane due to the balance of the influence of the polyp and the boundary conditions. This indicates that the model is valid in a structural sense, and is suitable for future in-depth studies of the effect of polyps on the free-vibration of vocal folds.

Future investigations with this code are concerned with the numerical prediction of the dynamic response of the vocal fold system coupled with the surrounding fluid and sound propagation. Transient acoustic radiation will then be computed and assessed with the pathological models to assess the effects of polyps on the radiated sound.

References

[1] F. Alipour, D. A. Berry, I. R. Titze. "A finite-element model of vocal-fold vibration." The Journal of the Acoustical Society of America, **108**, 3003–3012 (2000).

[2] M. de Oliveira Rosa, J. C. Pereira, M. Grellet, A. Alwan. "A contribution to simulating a three-dimensional larynx model using the finite element method." The Journal of the Acoustical Society of America, **114**, 2893–2905 (2003).

[3] S. Deguchi, Y. Kawahara. "Simulation of human phonation with vocal nodules." American Journal of Computational Mathematics, **1**, 189–201 (2011).

[4] P. Bhattacharya, T. H. Siegmund. "A canonical biomechanical vocal fold model." Journal of Voice, **26**, 535–547 (2012).

[5] D. J. Daily, S. L. Thomson. "Acoustically-coupled flow-induced vibration of a computational vocal fold model." Computers & structures, **116**, 50–58 (2013).

[6] H. E. Gunter. "A mechanical model of vocal-fold collision with high spatial and temporal resolution." The Journal of the Acoustical Society of America, **113**, 994–1000 (2003).

[7] T. E. Shurtz, S. L. Thomson. "Influence of numerical model decisions on the flow-induced vibration of a computational vocal fold model." Computers & structures, **122**, 44–54 (2013).

[8] S. L. Thomson, L. Mongeau, S. H. Frankel. "Aerodynamic transfer of energy to the vocal folds." The Journal of the Acoustical Society of America, **118**, 1689–1700 (2005).

[9] K. Ishizaka, J. L. Flanagan. "Synthesis of voiced sounds from a two-mass model of the vocal cords." Bell system technical journal, **51**, 1233–1268 (1972).

[10] I. R. Titze. "The human vocal cords : A mathematical model part I." Phonetica, **28**, 129–170 (1973).

[11] I. R. Titze. "The human vocal cords : A mathematical model part II." Phonetica, **29**, 1–21 (1974).

[12] K. Ishizaka, N. Isshiki. "Computer simulation of pathological vocal-cord vibration." The Journal of the Acoustical Society of America, **60**, 1193–1198 (1976).

[13] I. Steinecke, H. Herzel. "Bifurcations in an asymmetric vocal-fold model." The Journal of the Acoustical Society of America, **97**, 1874–1884 (1995).

[14] B. D. Erath, M. Zañartu, S. D. Peterson, M. W. Plesniak. "Nonlinear vocal fold dynamics resulting from asymmetric fluid loading on a two-mass model of speech." Chaos : An Interdisciplinary Journal of Nonlinear Science, **21**, 033113 (2011).

[15] N. Wan, D. Peng, M. Sun, D. Zhang. "Nonlinear oscillation of pathological vocal folds during vocalization." Science China Physics, Mechanics and Astronomy, **56**, 1324–1328 (2013).

[16] Y. Zhang, J. J. Jiang. "Chaotic vibrations of a vocal fold model with a unilateral polyp." The Journal of the Acoustical Society of America, **115**, 1266–1269 (2004).

[17] B. H. Story, I. R. Titze. "Voice simulation with a body-cover model of the vocal folds." The Journal of the Acoustical Society of America, **97**, 1249–1260 (1995).

[18] C. Tao, J. J. Jiang, Y. Zhang. "Simulation of vocal fold impact pressures with a self-oscillating finite-element model." The Journal of the Acoustical Society of America, **119**, 3987–3994 (2006).

[19] C. Tao, J. J. Jiang. "Mechanical stress during phonation in a self-oscillating finite-element vocal fold model." Journal of biomechanics, **40**, 2191–2198 (2007).

[20] C. Tao, J. J. Jiang. "Anterior-posterior biphonation in a finite element model of vocal fold vibration." The Journal of the Acoustical Society of America, **120**, 1570–1577 (2006).

[21] B. Erath, M. Plesniak. "Three-dimensional laryngeal flow fields induced by a model vocal fold polyp." International Journal of Heat and Fluid Flow, **35**, 93–101 (2012).

[22] H. E. Gunter, R. D. Howe, S. M. Zeitels, J. B. Kobler, R. E. Hillman. "Measurement of vocal fold collision forces during phonation : Methods and preliminary data." Journal of Speech, Language, and Hearing Research, **48**, 567–576 (2005).

[23] J. E. Kelleher, T. Siegmund, M. Du, E. Naseri, R. W. Chan. "Empirical measurements of biomechanical anisotropy of the human vocal fold lamina propria." Biomechanics and modeling in mechanobiology, **12**, 555–567 (2013).

[24] K. K. Gupta. *STARS : A general-purpose finite element computer program for analysis of engineering structures*, volume 1129 (National Aeronautics and Space Administration, Scientific and Technical Information Branch, 1984).

[25] D. A. Berry, I. R. Titze. "Normal modes in a continuum model of vocal fold tissues." The Journal of the Acoustical Society of America, **100**, 3345–3354 (1996).

[26] H.Luo, R.Mittal, X.Zheng, S.A.Bielamowicz, R.J.Walsh, J.K.Hahn. "An immersed-boundary method for flow-structure interaction in biological systems with application to phonation." Journal of Computational Physics, **227**, 9303–9332 (2008).

[27] M. Petyt. *Introduction to finite element vibration analysis* (Cambridge University Press, 1990).

[28] MATLAB. *version 8.1.0.604 (R2013a)* (The Mathworks Inc., Natick, Massachusetts, 2013).

[29] T. Yang. *Finite element structural analysis* (Prentice-Hall Englewood Cliffs, New Jersey, 1986).

[30] O. Zienkiewicz. *The finite element method* (McGraw-Hill Book Company, 1977).

[31] K.-J. Bathe. *Finite element procedures* (Prentice-Hall Englewood Cliffs, New Jersey, 1996).

[32] H. D. Jiang J.J., Diaz C.E. "Finite element modeling of vocal fold vibration in normal phonation and hyperfunctional dysphonia : Implications for the pathogenesis of vocal nodules." Annals of Otology, Rhinology, and Laryngology, **107**, 603–610 (1998).

[33] C. A. Rosen, J. Gartner-Schmidt, B. Hathaway, C. B. Simpson, G. N. Postma, M. Courey, R. T. Sataloff. "A nomenclature paradigm for benign midmembranous vocal fold lesions." The Laryngoscope, **122**, 1335–1341 (2012).

[34] R. Mittal, B. D. Erath, M. W. Plesniak. "Fluid dynamics of human phonation and speech." Annual Review of Fluid Mechanics, **45**, 437–467 (2013).

[35] V. Uloza, M. Kaseta, R. Pribuisiene, V. Saferis, V. Jokūzis, A. Gelzinis, M. Bacauskiene. "Quantitative microlaryngoscopic measurements of vocal fold polyps, glottal gap and their relation to vocal function." Medicina (Kaunas), **44**, 266–272 (2008).

[36] L. Wallis, C. Jackson-Menaldi, W. Holland, A. Giraldo. "Vocal fold nodule vs. vocal fold polyp : answer from surgical pathologist and voice pathologist point of view." Journal of Voice, **18**, 125–129 (2004).